

# Numerical simulation of the fouling process

Fahmi Brahim, Wolfgang Augustin, Matthias Bohnet \*

*Institut für Chemische und Termische Verfahrenstechnik, Technische Universität Braunschweig, Langer Kamp 7, 38106 Braunschweig, Germany*

Received 21 January 2002; accepted 13 March 2002

## Abstract

Fouling of heat transfer surfaces causes serious technical and economic problems in industry. The goal of this work is to simulate the aforementioned fouling process using the CFD code FLUENT. The obtained numerical results assist in designing and running heat exchangers.

Based on models for the calculation of deposition and removal mass rates [S. Krause, *Internat. Chem. Engrg.* 33 (1993)], the crystallization fouling of calcium sulfate on flat heat transfer surfaces was simulated. The induction period, which occurs with almost all fouling processes, was therefore not considered.

The simulation of real crystal growth requires a continuous variation of the geometric flow model and therefore considerable computational effort. For that reason fictitious crystal growth was simulated instead. This numerical simplification enabled an unsteady simulation to be obtained, of the fouling process and a realistic description of the temporal modification of both the flow and temperature field due to the continuous crystal growth.

Based on experimental results of Hirsch [M. Bohnet et al., in: T.R. Bott et al. (Eds.), *Understanding Heat Exchanger Fouling and its Mitigation*, United Engineering Foundation and Begell House, New York, 1997, pp. 201–208], a model was developed which enables the calculation of the density of the fouling layer not only as a function of the local position within the fouling layer, but also as a function of the time-dependent total thickness of the fouling layer. In addition a model was developed, that enables a realistic distribution of the heat flux along the heat transfer surface during the simulation. Both models provide a more exact description of the complicated fouling process.

Results of the numerical simulation are the prediction of the fouling resistance as a function of time and the calculation of the temperature distribution within the fouling layer. In view of the complexity of the fouling process during the incrustation of heat transfer surfaces and the fact that not all influences from the used models could be considered the agreement between calculated and experimentally obtained data is satisfactory.

© 2002 Éditions scientifiques et médicales Elsevier SAS. All rights reserved.

*Keywords:* Heat and mass transfer; Crystallization fouling; Modeling; Numerical simulation; CFD

## 1. Introduction

An analytical description resulting from complex combinations of different fouling mechanisms is not yet possible. Models have been developed at the University of Braunschweig for single fouling mechanisms such as crystallization (Fig. 1) or sedimentation. These models have been added to a CFD code for the numerical simulation of heat and mass transfer. The results enable a fast and prediction of the fouling behaviour.

In a preliminary calculation the simple case of parallel flow across flat plates is investigated. Using this simplifi-

cation numerous fouling experiments under different conditions were calculated. The measurements were taken using aqueous solutions of  $\text{CaSO}_4$  and serve as a verification of the numerical simulation.

## 2. Experimental Set-up

Fig. 2 is a schematic diagram of the experimental unit used for the fouling experiments. The centerpiece of the experimental set-up consists of three measuring sections. The second and third test sections are annular test tubes used for reference measurements. The first test section includes a plate heat exchanger suited for a comfortable replacement of its heat transfer surface. The salt concentration of the aqueous calcium sulphate solution is controlled by conduction

\* Corresponding author.

*E-mail addresses:* [f.brahim@tu-bs.de](mailto:f.brahim@tu-bs.de) (F. Brahim),  
[w.augustin@tu-bs.de](mailto:w.augustin@tu-bs.de) (W. Augustin), [m.bohnet@tu-bs.de](mailto:m.bohnet@tu-bs.de) (M. Bohnet).

## Nomenclature

$a_1, \dots, a_8$	constant	$T_F$	temperature of salt solution . . . . . K
$A_1, \dots, A_4$	constant	$T_w$	temperature of heat transfer surface . . . . . K
$c_F$	concentration of salt solution . . . . . $\text{kg}\cdot\text{m}^{-3}$	$U$	flow velocity . . . . . $\text{m}\cdot\text{s}^{-1}$
$c_S$	saturation concentration . . . . . $\text{kg}\cdot\text{m}^{-3}$	$U_\tau$	friction velocity . . . . . $\text{m}\cdot\text{s}^{-1}$
$c_f$	concentration in the vicinity of the fouling layer . . . . . $\text{kg}\cdot\text{m}^{-3}$	$x_f$	thickness of crystal layer . . . . . m
$D$	diffusion coefficient . . . . . $\text{m}^2\cdot\text{s}^{-1}$	$y$	wall distance . . . . . m
$d_h$	hydraulic diameter . . . . . m	$w$	fluid velocity above the fouling layer . . . . . $\text{m}\cdot\text{s}^{-1}$
$d_p$	mean crystal diameter . . . . . m	$w_e$	mean inlet velocity . . . . . $\text{m}\cdot\text{s}^{-1}$
$E$	activation energy . . . . . $\text{J}\cdot\text{mol}^{-1}$	$\delta$	linear expansion coefficient . . . . . $\text{K}^{-1}$
$g$	gravitational acceleration . . . . . $\text{m}\cdot\text{s}^{-2}$	$\Delta t$	computing time step . . . . . s
$H$	height of the flow channel . . . . . m	$\Delta T$	temperature gradient . . . . . K
$P/K$	cohesion coefficient . . . . . $\text{kg}\cdot\text{m}\cdot\text{s}^{-2}$	$\Delta_L H_0$	solution enthalpy . . . . . $\text{J}\cdot\text{mol}^{-1}$
$k_0$	overall heat transfer coefficient (clean heat exchanger surface) . . . . . $\text{W}\cdot\text{m}^{-2}\cdot\text{K}^{-1}$	$\Delta c_p$	difference of heat capacity . . . . . $\text{J}\cdot\text{mol}^{-1}\cdot\text{K}^{-1}$
$k_f$	overall heat transfer coefficient (fouled heat exchanger surface) . . . . . $\text{W}\cdot\text{m}^{-2}\cdot\text{K}^{-1}$	$\rho$	density of salt solution . . . . . $\text{kg}\cdot\text{m}^{-3}$
$k_R$	rate of reaction (here: 2nd order) . . . . . $\text{m}^4\cdot\text{kg}\cdot\text{s}^{-1}$	$\rho_f$	density of fouling layer . . . . . $\text{kg}\cdot\text{m}^{-3}$
$\dot{m}$	total mass rate . . . . . $\text{kg}\cdot\text{m}^{-2}\cdot\text{s}^{-1}$	$\lambda_f$	thermal conductivity of fouling layer . . . . . $\text{W}\cdot\text{m}^{-1}\cdot\text{K}^{-1}$
$\dot{m}_d$	deposition mass rate . . . . . $\text{kg}\cdot\text{m}^{-2}\cdot\text{s}^{-1}$	$\beta$	mass transfer coefficient . . . . . $\text{m}\cdot\text{s}^{-1}$
$\dot{m}_r$	removal mass rate . . . . . $\text{kg}\cdot\text{m}^{-2}\cdot\text{s}^{-1}$	$\nu$	kinematic viscosity . . . . . $\text{m}^2\cdot\text{s}^{-1}$
$n$	number of wall cells along the heat transfer surface	$\eta$	dynamic viscosity . . . . . $\text{kg}\cdot\text{m}^{-1}\cdot\text{s}^{-1}$
$P$	intercrystalline adhesion force . . . . . N	$k$	turbulent kinetic energy . . . . . $\text{m}^2\cdot\text{s}^{-2}$
$\dot{q}$	heat flux . . . . . $\text{W}\cdot\text{m}^{-2}$	$\varepsilon$	dissipation rate of tubulent kinetic energy . . . . . $\text{m}^2\cdot\text{s}^{-3}$
$R_f$	fouling resistance . . . . . $\text{W}\cdot\text{m}^{-2}\cdot\text{K}^{-1}$	$Re$	Reynolds number
$T_f$	temperature of fouling layer surface . . . . . K	$Sh$	Sherwood number
		$Sc$	Schmidt number

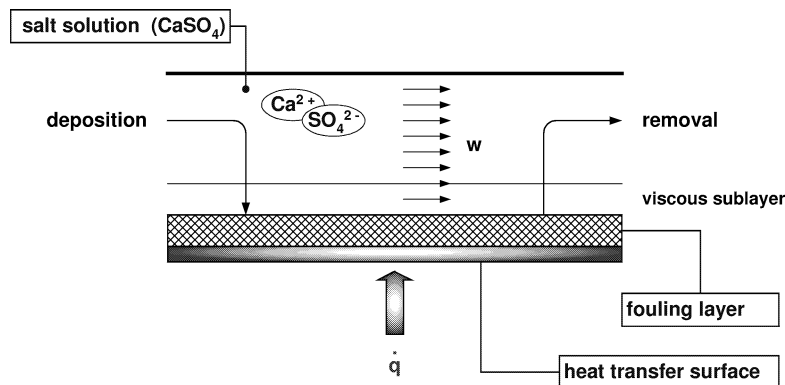


Fig. 1. Processes of crystallization fouling on heat transfer surfaces.

measurement. Two centrifugal pumps provide a continuous flow of liquid through the system. The solution is passed from a storage tank through a heat exchanger, which controls the inlet temperature and then to the measuring sections. The filter avoids sedimentation of particles and secondary nucleation in the test sections, since seed particles can influence considerably nucleation behaviour. The heat exchanger guarantees a constant inlet temperature at the test sections. The liquid flow is divided and flows to the two measuring sections, each equipped with a flowmeter and a

flow controller. After passing through the two measuring sections the two partial streams are recombined and fed back to the storage tank. Due to a relatively large volume of liquid in the storage tank, the decline of the concentration of salt in the solution throughout the fouling period is rather low. Regular addition of calcium sulfate hemihydrate to the storage tank maintains a relatively constant concentration. The heat exchanger surfaces of the measuring sections are heated electrically allowing for operation at constant heat flux.

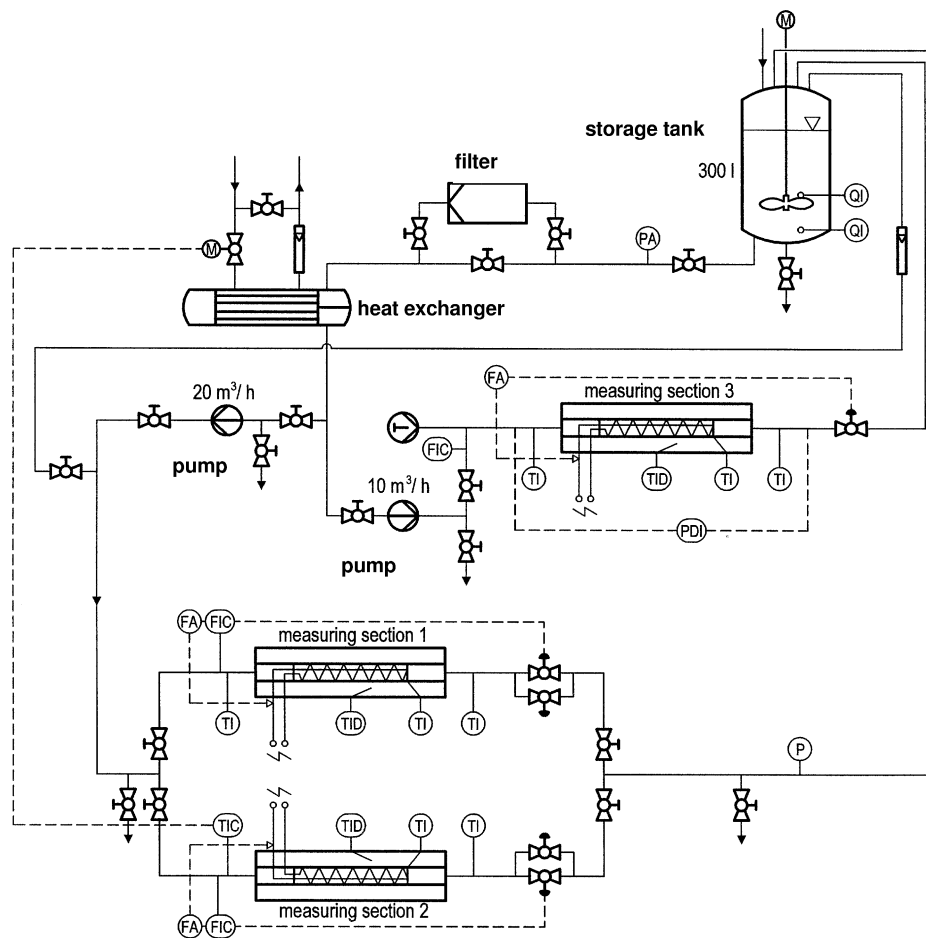


Fig. 2. Experimental Set-up.

### 3. Geometrical flow model

The geometrical flow model shown in Fig. 3 represents a rectangular gap which corresponds to the measuring Section 1 of the fouling test unit.

Results of 2D and 3D simulations regarding of flow velocity and surface temperature distribution were almost identical. Since the computational effort and cost in terms of CPU time and memory of the 3D simulation is very high, the flow case was regarded as two-dimensional.

The discretization of the computing area was performed with a structured grid. In the case of channel and pipe flows, where large modifications of the flow variables mainly occur perpendicular to the wall, the structured grid offers the following two advantages compared to the unstructured grid [3]:

- (1) The square cells of the structured grid enable stable calculation and faster convergence.
- (2) The structured grid allows an aspect ratio up to 10 which translates into saving grid cells thus maximizing computer capacity. Such an aspect ratio with an unstructured grid leads to considerable distortion of the cells and thus to instabilities and inaccuracies within the simulation.

### 4. Turbulence model and modeling of the wall region

FLUENT provides many choices of turbulence models. The simplest “complete models” of turbulence are two-equation models in which the solution from two separate transport equations allows the turbulent velocity and length scales to be independently determined. The  $k-\epsilon$  models fall within this class of turbulence models. Robustness, economy and reasonable accuracy for a wide range of turbulent flows explain their popularity in industrial flow and heat transfer simulations. They are semi-empirical models and the derivation of the model equations relies on phenomenological considerations and empiricism. By the numerical simulation the realizable  $k-\epsilon$  model was used. It offers the following advantages compared to the standard model:

- (1) The possibility of application not only to high Reynolds-number flows ( $Re > 50000$ ) but also with small Reynolds-number and transient flows ( $2300 < Re < 10000$ ).
- (2) The realizable  $k-\epsilon$  model satisfies certain mathematical constraints on the Reynolds stresses, consistent with the physics of turbulent flows.

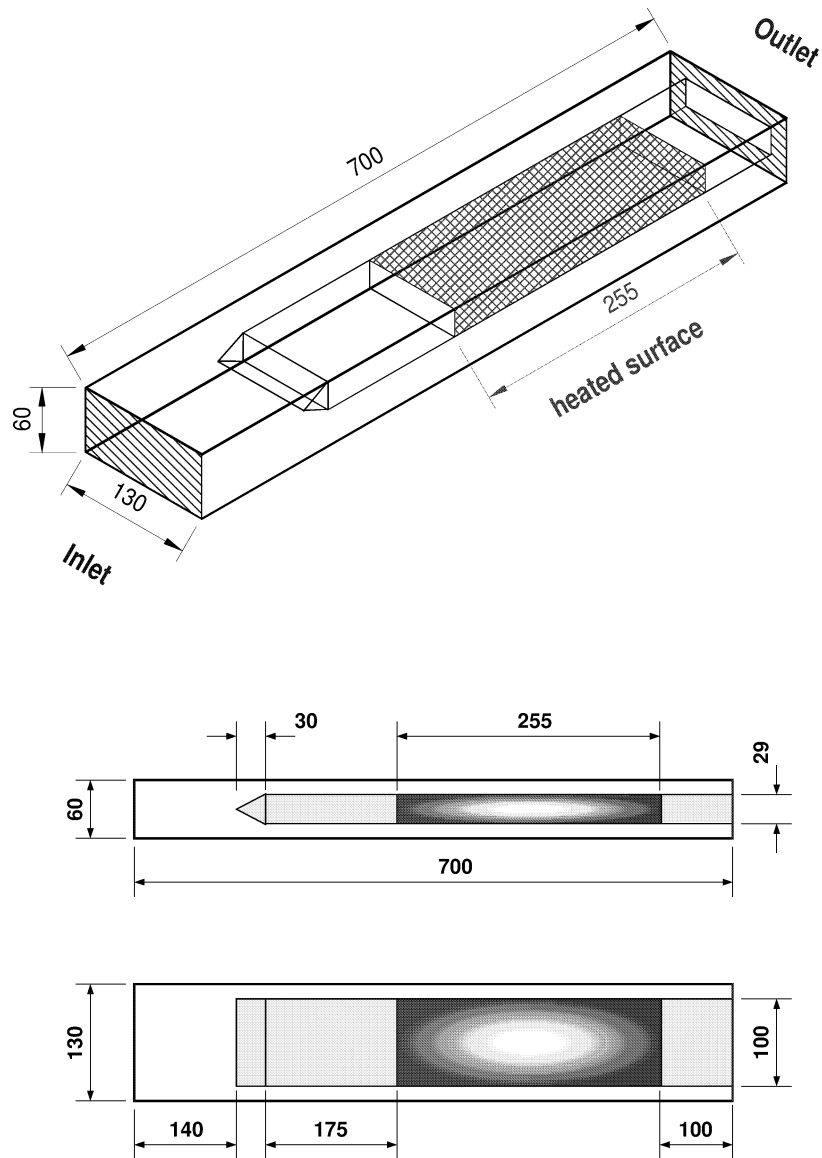


Fig. 3. Geometrical flow model.

The turbulence models are valid primarily for turbulent core flows (i.e., the flow in the regions somewhat far from walls). Therefore consideration needs to be given to an adaption for wall-bounded flows (Fig. 4).

There are two approaches for modeling the near-wall region. In one approach the viscosity affected inner region (viscous sublayer and buffer layer) is not resolved. Instead, semi-empirical formulae called wall functions, are used to bridge the viscosity affected region between the wall and the fully-turbulent region. In the second model, named the “two-layer zonal model”, the wall functions are completely abandoned in favour of resolving the viscosity affected near-wall region all the way to the viscous sublayer. In the two-layer model, the entire domain is subdivided into a viscosity affected region and a fully turbulent region (Fig. 5).

The wall function approach, however, is inadequate in situations where the low-Reynolds number ( $Re < 10000$ )

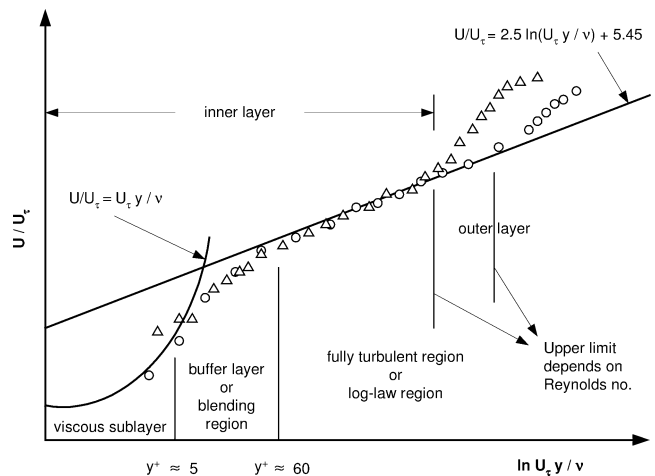


Fig. 4. Subdivisions of the Near-Wall Region [3].

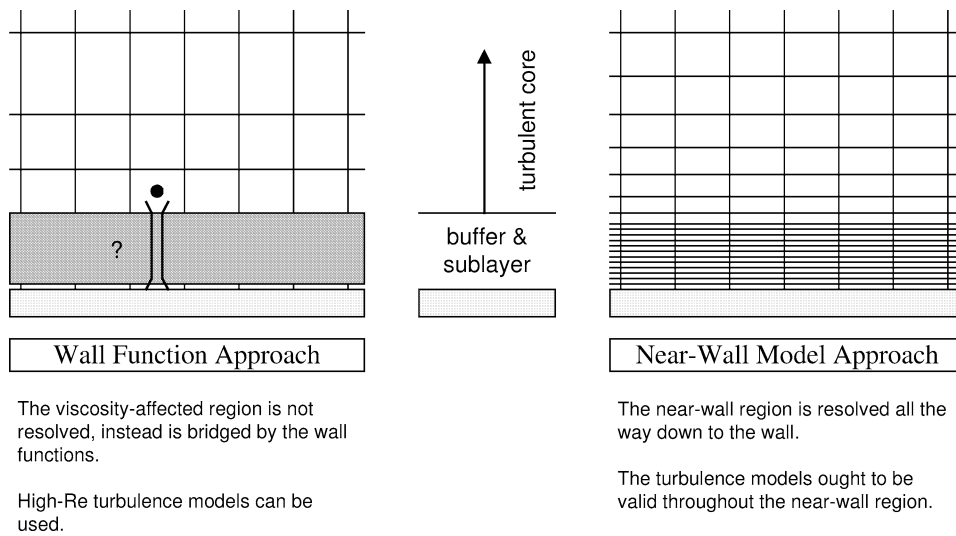


Fig. 5. Near-wall treatments in Fluent [3].

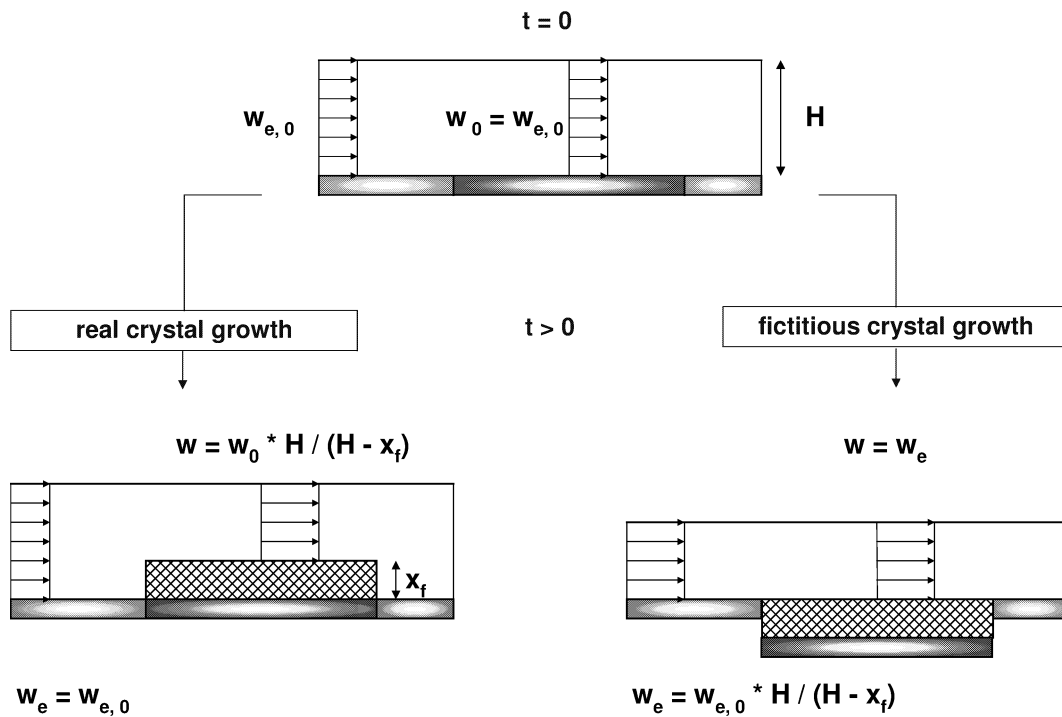


Fig. 6. Schematic presentation of the fictitious crystal growth.

effects are pervasive throughout the flow domain in question, and therefore the hypotheses underlying the wall functions cease to be valid. Such situations require near-wall models that are valid in the viscosity affected region and accordingly integrable all the way to the wall.

### 5. Simulation of the crystallization

For the numerical simulation of crystal growth to be possible the geometry of the flow model has to be permanently modified. This process is very complex and requires a con-

siderable computational effort. A solution for this problem is offered by the simulation of the fictitious crystal growth, whose principle is shown in Fig. 6.

In the upper part of Fig. 6 the flow channel of the height  $H$  is represented.  $w_{e,0}$  is the mean inlet velocity. At  $t = 0$  h there is no crystal layer has yet grown. The mean flow velocity  $w_0$  above the heat transfer surface is equal to the mean inlet velocity. In a real case scenario, a fouling layer of the thickness  $x_f$  grows after a certain time  $t$ . The inlet velocity remains unchanged and is equal to the inlet velocity at  $t = 0$  h:

$$w_e = w_{e,0} \tag{1}$$

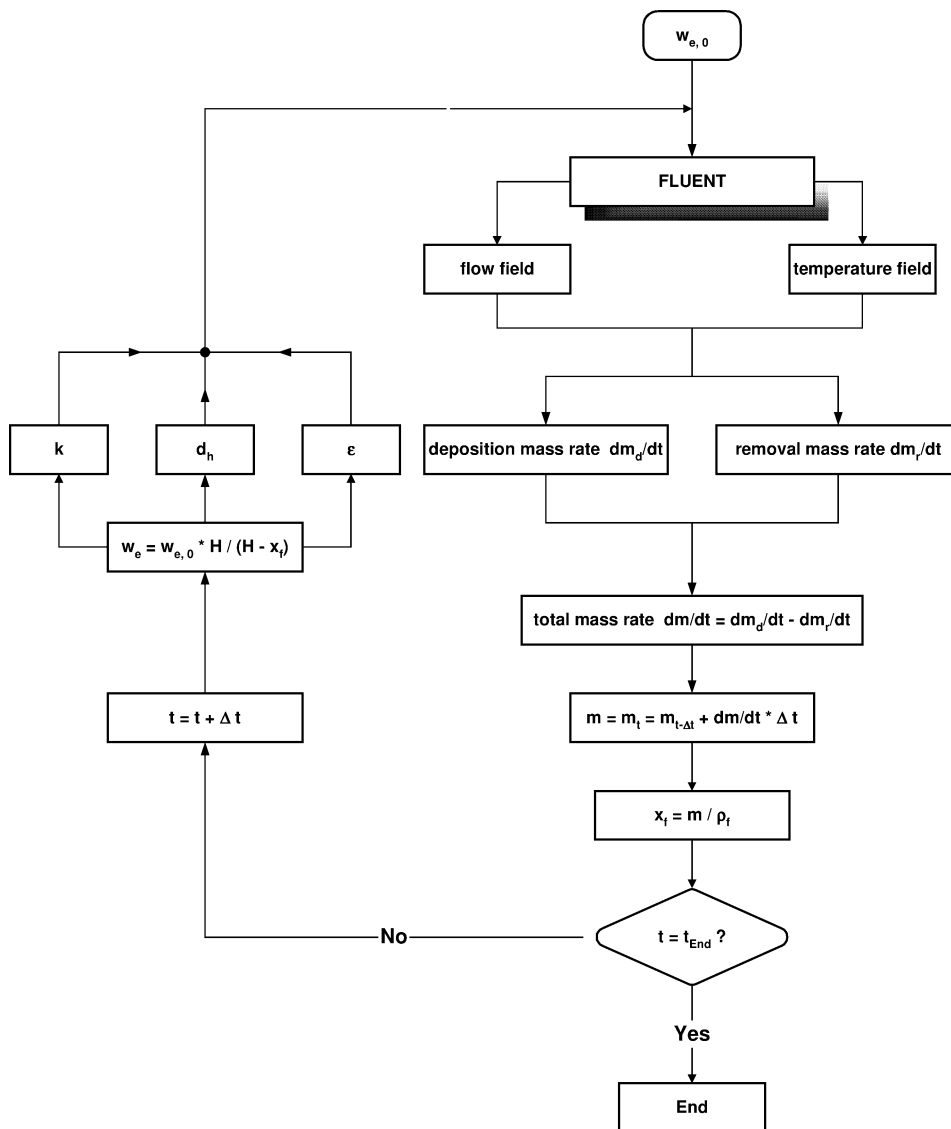


Fig. 7. Explanation of the calculation steps for the simulation of the fictitious crystal growth.

The flow velocity above the crystal layer increases, however, due to the narrowed cross section and is calculated based on continuity conditions as:

$$w = w_0 \cdot \frac{H}{H - x_f} \quad (2)$$

During the simulation of the fictitious crystal growth, the inlet velocity is increased based on the calculated value of the thickness of the crystal layer:

$$w_e = w_{e,0} \cdot \frac{H}{H - x_f} \quad (3)$$

Consequently, the mean flow velocity increases above the heat transfer surface with time. A modification of the hydraulic diameter must be considered due to the fictitious cross section narrowing. Therefore a sufficiently realistic description of the flow and temperature field above the fictitious fouling layer was achieved. The principle of the

fictitious crystal growth can be described more detailed with the help of the flow chart in Fig. 7.

At the start of the simulation an inlet velocity  $w_{e,0}$  is defined as a boundary condition. Fluent calculates, based on this velocity and other boundary conditions, the flow and temperature field. The temperature along the heat transfer surface enables the calculation of the deposition and removal rates, i.e., the deposit that accumulates or is removed from unit area per unit time from the fouling layer.

In a further step the total mass rate is calculated as a difference between deposition and removal mass rates:

$$\frac{dm}{dt} = \frac{dm_d}{dt} - \frac{dm_r}{dt} \implies \dot{m} = \dot{m}_d - \dot{m}_r \quad (4)$$

The crystal mass per surface area at a determined time  $t + \Delta t$  is calculated as a sum of the total mass per surface area

at time  $t$  added to the calculated mass rate during the new computing time step  $\Delta t$ :

$$m_{t+\Delta t} = m_t + \frac{dm}{dt} \cdot \Delta t = m_t + \dot{m} \cdot \Delta t \quad (5)$$

The time step was adjusted in all simulation calculations to  $\Delta t = 1 \text{ h} = 3600 \text{ s}$  which is sufficiently short for the description of the fouling process.

The thickness of the fouling layer is then calculated as the total deposit mass per surface area divided by the density  $\rho_f$  of the fouling layer:

$$x_f = \frac{m_{t+\Delta t}}{\rho_f} \quad (6)$$

### 5.1. Model for the calculation of the deposition mass rate

By numerical calculation of the deposition mass rate  $\dot{m}_d$  the mass transfer resistance between bulk and interface salt solution/crystal layer was considered. Thus the concentration profile in the bulk and in the laminar boundary layer can be presented as shown in Fig. 8.

In the first step the calcium and sulfate ions are transported from the bulk to the interface by diffusion. The mass transfer process is caused by the concentration gradient  $\Delta c_1 = c_F - c_f$ :

$$\dot{m}_d = \beta \cdot (c_F - c_f) \quad (7)$$

In the second step the ions are built into the crystal lattice. The concentration gradient  $\Delta c_2 = (c_f - c_S)$  is responsible for the building process. Investigations of Konak [4] showed that the order of the surface reaction corresponds to the number of ions ( $\text{Ca}^{++}$  und  $\text{SO}_4^{--}$ ) that take part in the crystallization reaction. The mass flux can therefore be calculated as follows:

$$\dot{m}_d = k_R \cdot (c_f - c_S)^2 \quad (8)$$

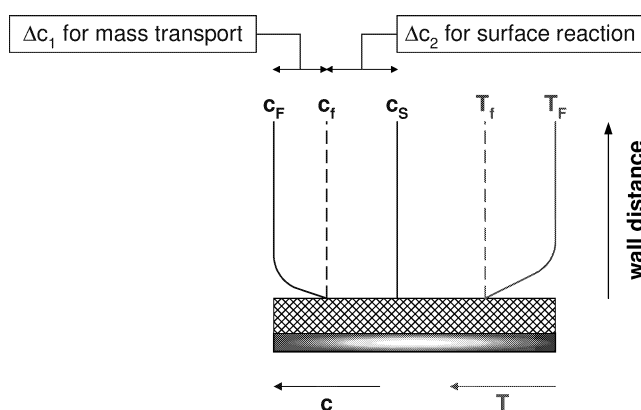


Fig. 8. Concentration and temperature profile in the vicinity of the fouling layer (fouling by crystallization).

$k_R$  is the surface reaction rate constant. It can be calculated using the Arrhenius approach:

$$k_R = k_{R0} \cdot e^{-\frac{E}{\mathfrak{R} \cdot T_f}} \quad (9)$$

The following values were taken for the constant of the concerned reaction  $k_{R0}$  and the reaction activation energy  $E$  [1]:

$$\begin{cases} k_{R0} = 7.07 \text{ m}^4 \cdot \text{kg}^{-1} \cdot \text{s}^{-1} \\ E = 37143 \text{ J} \cdot \text{mol}^{-1} \end{cases}$$

$T_f$  defines the surface temperature of the fouling layer (Fig. 8).  $c_S$  is the saturation concentration and was calculated as a function of  $T_f$  [5]:

$$\log(c_S) = -\frac{\Delta_L H_0}{2.3 \cdot \mathfrak{R} \cdot T_f} + \frac{\Delta c_P}{\mathfrak{R}} \cdot \log(T_f) + C \quad (10)$$

If it is assumed that all ions transported to the phase boundary participate in the surface reaction, the equations can then be used for the calculation of the mass rates of transport and incorporation into the fouling layer by eliminating the unknown concentration  $c_f$  at the phase boundary. The combination of Eqs. (7) and (8) leads to the model equation for the calculation of the deposition mass rate:

$$\dot{m}_d = \beta \cdot \left[ \frac{1}{2} \cdot \frac{\beta}{k_R} + \Delta c - \left( \frac{1}{4} \cdot \left( \frac{\beta}{k_R} \right)^2 + \frac{\beta}{k_R} \cdot \Delta c \right)^{1/2} \right] \quad (11)$$

where  $\Delta c$  is the total concentration gradient:

$$\Delta c = \Delta c_1 + \Delta c_2 = c_F - c_S \quad (12)$$

The mass transfer coefficient can be determined as a function of the Sherwood number and the diffusion coefficient:

$$\beta = \frac{Sh \cdot D}{d_h} \quad (13)$$

A semiempirical approach according to Lammers [5] was used for calculating of the Sherwood number:

$$Sh = 0.034 \cdot Re^{0.875} \cdot Sc^{1/3} \quad (14)$$

with

$$Sh = \frac{\beta \cdot d_h}{D}, \quad Re = \frac{w \cdot d_h \cdot \rho}{\eta}, \quad Sc = \frac{\eta}{\rho \cdot D} \quad (15)$$

In order to determine the diffusion coefficient of calcium sulfate in aqueous solution a computational model based on calculated results of Lammers [5] was developed. This model describes the dependency of the diffusion coefficient on the two parameters: temperature and concentration (Table 1):

$$D(T, c) = \frac{a_1 \cdot T^3 + a_2 \cdot T^2 + a_3 \cdot T + a_4}{c + 1} + a_5 \cdot T^3 + a_6 \cdot T^2 + a_7 \cdot T + a_8 \quad (16)$$

Table 1  
Model coefficients for the calculation of the diffusion coefficient Eq. (16)

a <sub>1</sub>	a <sub>2</sub>	a <sub>3</sub>	a <sub>4</sub>	a <sub>5</sub>	a <sub>6</sub>	a <sub>7</sub>	a <sub>8</sub>
$3.923 \times 10^{-16}$	$2.333 \times 10^{-15}$	$7.153 \times 10^{-12}$	$1.049 \times 10^{-10}$	$-2.539 \times 10^{-16}$	$1.087 \times 10^{-13}$	$1.036 \times 10^{-11}$	$2.769 \times 10^{-10}$

### 5.2. Model for the calculation of the removal mass rate

The following approach was used in the calculation of the removal mass rate [6]:

$$\dot{m}_r = \frac{K}{P} \cdot \rho_f \cdot (1 + \delta \cdot \Delta T) \cdot d_p \cdot (\rho^2 \cdot \eta \cdot g)^{1/3} \cdot x_f \cdot w^2 \quad (17)$$

The mean flow velocity  $w$  above the crystal layer can be calculated with Eq. (2).  $P$  describes the intercrystalline adhesion forces.  $K$  is a parameter that is equal to the number of fault points in the fouling layer. Based on his own measurements Krause suggested the following approach for the calculation of  $P/K$  [1]:

$$\frac{P}{K} = 83.2 \cdot w^{0.54} \quad (18)$$

$\rho_f$  is the mean density of the fouling layer. It can be determined as a function of the total calculated mass per unit area and the calculated mean thickness  $x_f$  of the fouling layer:

$$\rho_f = \frac{m}{x_f} \quad (19)$$

$(1 + \delta \cdot \Delta T)$  describes the temperature stresses in the fouling layer.  $\delta$  is the linear expansion coefficient and  $\Delta T$  the temperature gradient in the fouling layer. Both can be determined during a simulation including the calculated thickness of the crystal layer, the adjusted heat flux and the thermal conductivity as follows:

$$\Delta T = T_w - T_f = R_f \cdot \dot{q} = \left( \frac{1}{k_f} - \frac{1}{k_0} \right) \cdot \dot{q} = \frac{x_f}{\lambda_f} \cdot \dot{q} \quad (20)$$

According to Krause [1], an average value of 36  $\mu\text{m}$  was used for the mean crystal diameter.

### 5.3. Calculation of total mass rate, layer thickness and fouling resistance

The total mass transfer rate  $\dot{m}$  is calculated as the difference between the deposition and removal mass rates (Eq. (4)). The results of the numerical simulation are shown in Fig. 9. The decrease of the deposition mass rate per unit time can be explained by considering the decrease in surface temperature of the fouling layer, i.e., the supersaturation at the interface is reduced. This occurs because of higher fluid velocities and therefore an improved heat transfer. The increase of the mass transfer coefficient due to the flow rate acceleration is very small and does not affect considerably the calculation of the deposition mass rate.

The removed mass rate increases with time. This increase can be explained after considering the increase in flow rate and the growth of the crystal layer around the heating element. The increase in flow rate contributes to the rise of the wall shear stress, while the growth of the crystal layer increases the temperature stress within the fouling layer.

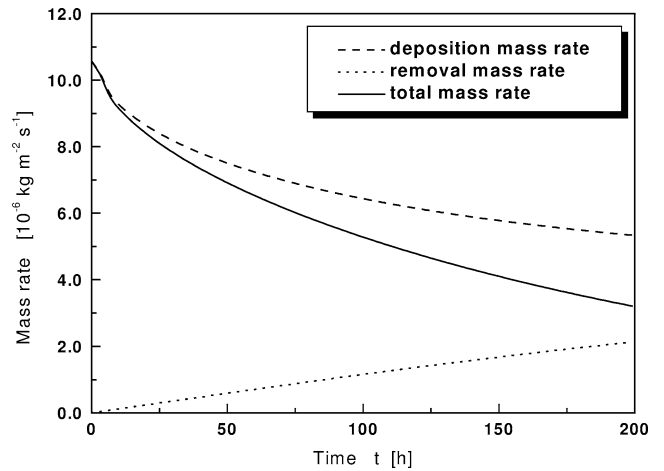


Fig. 9. Temporal change of deposition, removal and total mass rate ( $w = 0.1 \text{ m}\cdot\text{s}^{-1}$ ,  $\dot{q} = 37 \text{ kW}\cdot\text{m}^{-2}$ ).

The calculation of the average total thickness of the fouling layer until the time  $t + \Delta t$  is similar to the calculation of the total mass per unit area (Eq. (5)). It is calculated as the sum of the average total thickness from time  $t$  and the new growth within the time step  $\Delta t$ :

$$x_{f,t+\Delta t} = x_{f,t} + \frac{\dot{m} \cdot \Delta t}{\rho_f} \quad (21)$$

With the determined total thickness and assuming constant thermal conductivity, the fouling resistance can then be calculated as:

$$R_{f,t+\Delta t} = \frac{x_{f,t+\Delta t}}{\lambda_f} \quad (22)$$

### 5.4. Model for the calculation of unsteady local values of the density of the fouling layer

The density of the fouling layer is one of the most important quantities for the calculation of the fouling resistance. It does not only affect the calculation of the removal mass rate but also the calculation of the layer thickness itself. A profile of a fouling layer shows that the layer is not homogenous. In most cases 4 layers can be differentiated (Fig. 10).

Hirsch [2] noticed that the density of the fouling layer depends not only on the local position in the layer but also on the total thickness of the crystal layer (Fig. 11). For the numerical simulation it is necessary to calculate both unsteady and local values of the density of the fouling layer because of the relationship between time and the calculated total thickness of the crystal layer.

Based on results of abrasion experiments [2] and neglecting the aging effect of the crystal layer, which occurs in almost all fouling processes [7], the following computer model was developed and integrated using the numerical simulation:

$$\rho_f(x_f, x_{f,\text{Tot}}) = A_2 + \frac{A_1 - A_2}{1 + 10^{((x_f - A_3)/A_4)}} \quad (23)$$

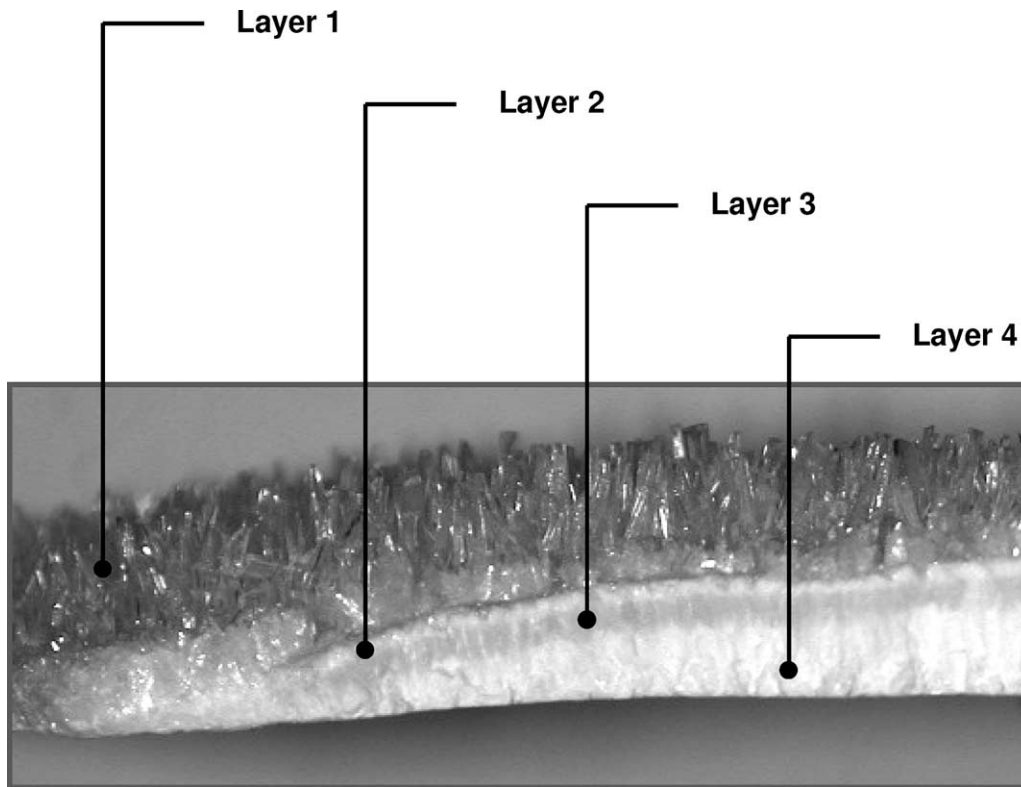


Fig. 10. Profile of a fouling layer.

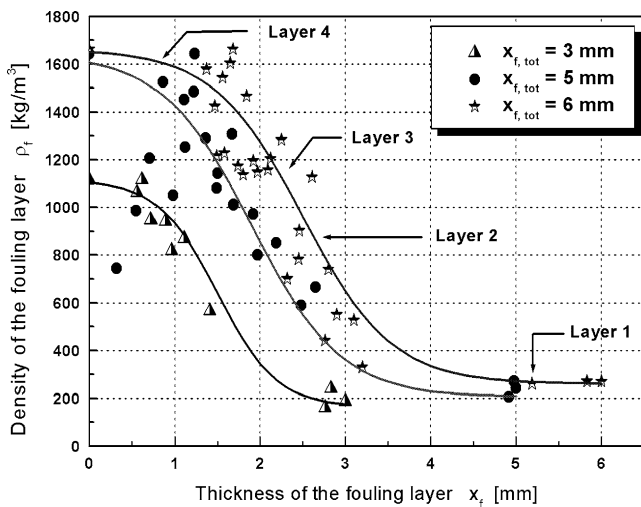


Fig. 11. Local density  $\rho_f$  for different total thicknesses of the fouling layer [2].

The coefficients  $A_1$ ,  $A_2$ ,  $A_3$  and  $A_4$  are all dependant on the total thickness of the fouling layer (Table 2).

5.5. Model for a realistic heat flux distribution

The last model, which was integrated into the numerical simulation, enables a realistic distribution of the heat flux along the heat transfer surface. The principle is shown in Fig. 12.

Table 2  
Model coefficients for the calculation of the density of the fouling layer Eq. (23)

$A_1$	$10^3 \cdot \log(1.11 + 0.7 \cdot x_{f,Tot})$
$A_2$	$105 + 22.5 \cdot x_{f,Tot}$
$A_3$	$0.5 \cdot x_{f,Tot}$
$A_4$	$0.25 \cdot x_{f,Tot}$

At  $t = 0$  h, before the formation of a fouling layer begins, the heat flux is constant along the heated surface:

$$\dot{q}_1 = \dot{q}_2 = \dots = \dot{q}_n = \dot{q}_0 \tag{24}$$

where  $\dot{q}_0$  is the heat flux adjusted at the start of the simulation as a boundary condition. After a time  $t > 0$  a fouling layer grows with a specific thickness distribution. In reality the heat flows through the section with the smallest thermal resistance. Therefore a local and unsteady heat flux distribution along the heat transfer surface occurs.

In order to consider this phenomenon, the minimum total thickness of the crystal layer is determined after every time step. An example of this is apparent in Fig. 12 above the first wall cell:

$$x_{f,Tot,min} = \min(x_{f,Tot,1}, x_{f,Tot,2}, \dots, x_{f,Tot,n}) \tag{25}$$

The maximum heat flux  $\dot{q}_{max}$  will flow through the wall cell with the thinnest crystal layer. Through each other cell flows

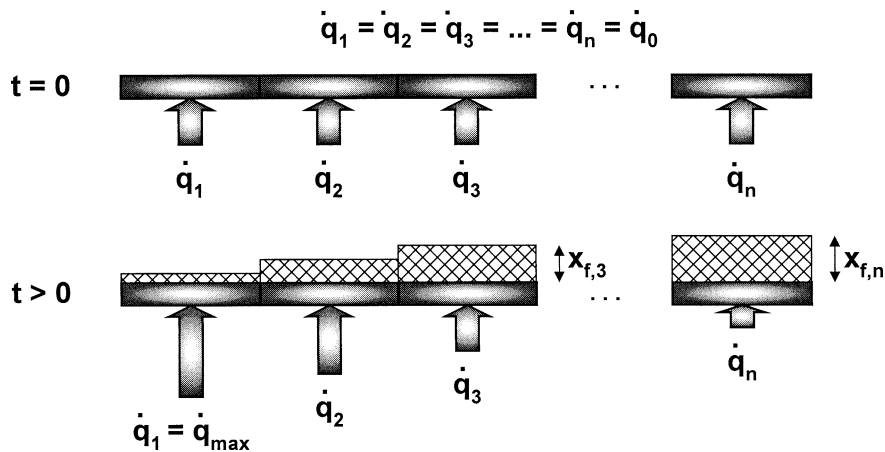


Fig. 12. Principle of the realistic distribution of the heat flux along the heat transfer surface.

a heat flux  $\dot{q}_i$ , which can be calculated as a function of the maximum heat flux and the crystal layer thickness ratio:

$$\dot{q}_i = \frac{x_{f,Tot,min}}{x_{f,Tot,i}} \cdot \dot{q}_{max} \quad (26)$$

Eq. (26) states that the larger the layer thickness  $x_{f,Tot,i}$  above the wall cell  $i$  the smaller the heat flux  $\dot{q}_i$  that flows through it.

Since Eq. (26) contains two unknown variables,  $\dot{q}_i$  and  $\dot{q}_{max}$ , a second equation is needed to provide a solution. The thermal balance along the heat transfer surface is stated below as:

$$\sum_{i=1}^n \dot{q}_i = n \cdot \dot{q}_0 \quad (27)$$

From the previous equation one can see that the total amount of heat remains the same regardless of the distribution of the heat flux. The combination of Eq. (26) and Eq. (27) results in:

$$\sum_{i=1}^n \frac{x_{f,Tot,min}}{x_{f,Tot,i}} \cdot \dot{q}_{max} = n \cdot \dot{q}_0 \quad (28)$$

the maximum heat flux has been therefore determined as:

$$\dot{q}_{max} = \frac{\sum_{i=1}^n \frac{x_{f,Tot,min}}{x_{f,Tot,i}}}{n} \cdot \dot{q}_0 \quad (29)$$

$\dot{q}_{max}$  from Eq. (29) can then be substituted in Eq. (26) in order to determine a unique heat flux for each wall cell depending on the thickness of the fouling layer. The determination of the heat flux distribution is made during the unsteady simulation after each time step, in order to describe realistically the influence of the growth of the fouling layer on the heat transfer surface.

## 6. Results

### 6.1. Comparison simulation/measurement

Fouling experiments with a constant calcium sulfate concentration of  $c_F = 2.42 \text{ g}\cdot\text{l}^{-1}$  and different flow rates and heat fluxes were carried out. Figs.13–16 show the measured and numerically calculated values of the fouling resistance versus time for four experiments with flow velocities between  $0.05$  and  $0.2 \text{ m}\cdot\text{s}^{-1}$  and different values of the heat flux.

The agreement between measurement and simulation is satisfactory. The form of the fouling curves can be reproduced by the simulation. Generally, the calculated values of the fouling resistance are smaller than the measured values.

### 6.2. Temperature distribution within the fouling layer

The numerical simulation enables an unsteady calculation of the temperature distribution within the fouling layer. These temperature values within the fouling layer at the location  $(i, j)$  according to Fig. 17 can be determined with the calculated surface temperature  $T_{f,i}$ , the adjusted heat flux  $\dot{q}_i$ , the calculated total thickness of the fouling layer  $x_{f,Tot,i}$  and by assuming a constant thermal conductivity  $\lambda_f$ :

$$T_{(i,j)} = T_{f,i} + \frac{x_{f,Tot,i} - x_{f,(i,j)}}{\lambda_f} \cdot \dot{q}_i \quad (30)$$

It was thereby assumed that the thermal conduction within the fouling layer takes place only perpendicularly to the heat transfer surface. A result of the numerical simulation is represented in Fig. 18.

Fig. 18 is a combined representation of the calculated thickness distribution of the fouling layer above the heat transfer surface and a contour representation of the temperature distribution within it.

The temperature increases from approximately  $80^\circ\text{C}$  at the phase boundary (salt solution/fouling layer) to more than  $260^\circ\text{C}$  in the vicinity of the heat transfer surface. The high temperatures reached cause generally a modification of

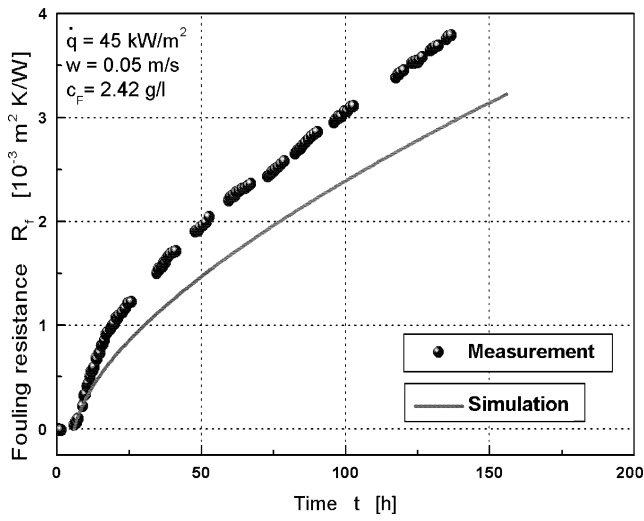


Fig. 13. Comparison of simulation and measurement results.

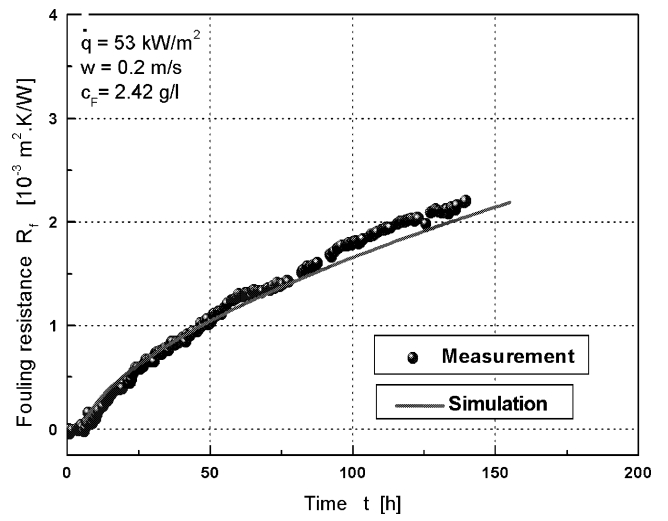


Fig. 16. Comparison of simulation and measurement results.

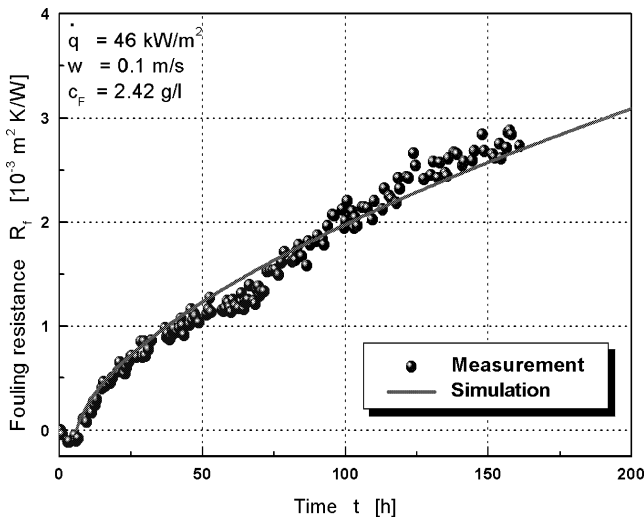


Fig. 14. Comparison of simulation and measurement results.

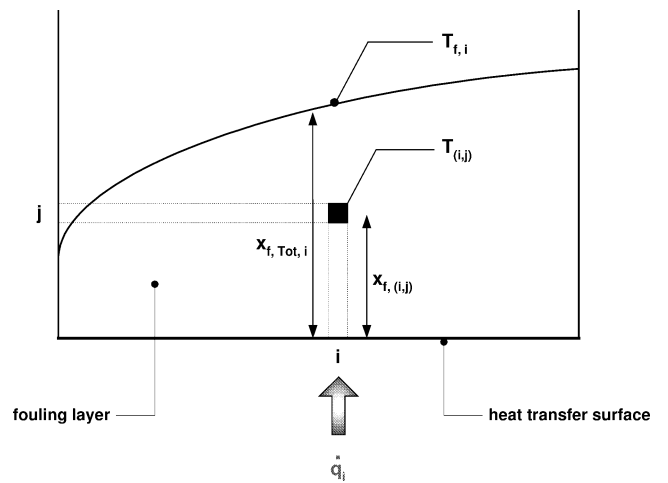


Fig. 17. Principle of the calculation of local temperature values within the fouling layer.

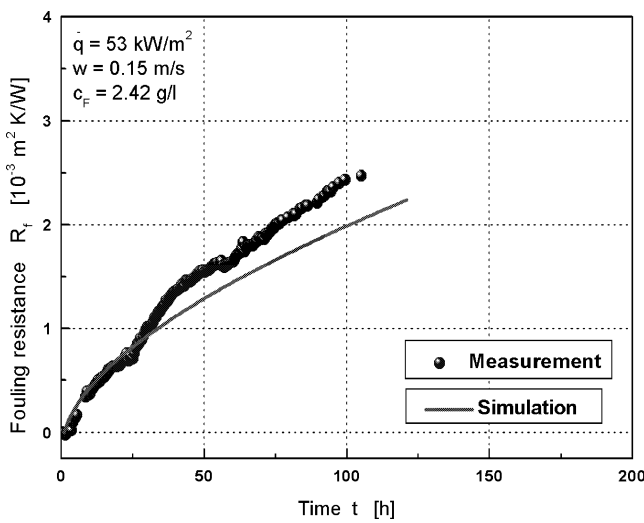


Fig. 15. Comparison of simulation and measurement results.

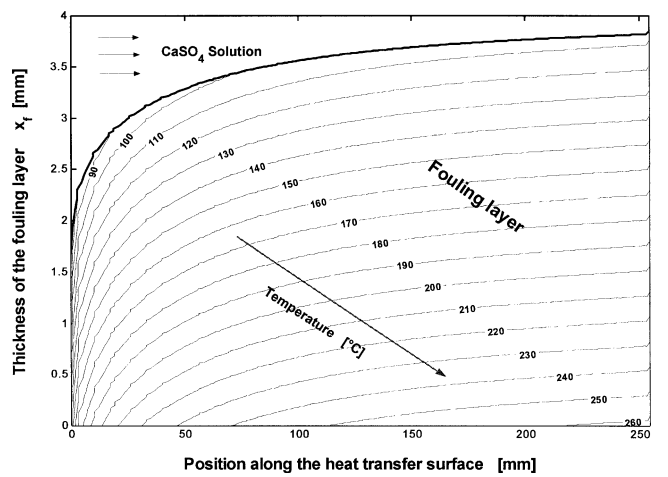


Fig. 18. Temperature distribution within the fouling layer.

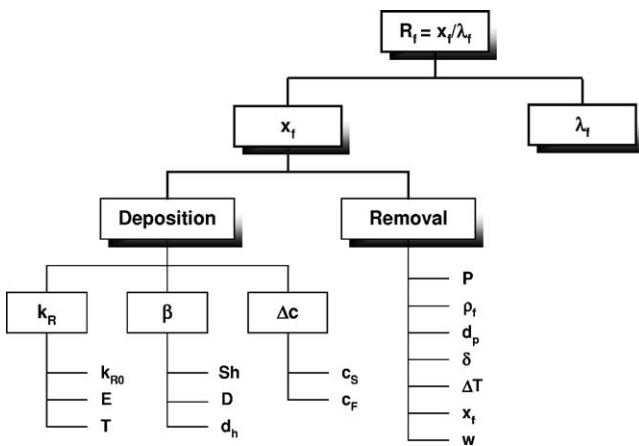


Fig. 19. Summary of the parameters which influence the numerical calculation of  $R_f$ .

the structure of the crystal (aging) which is also visible in Fig. 10.

## 7. Conclusion and prospect

In order to obtain a better agreement between observed behavior and calculation, the simulation of the real crystal growth has to be integrated in a numerical calculation to enable a variation of the geometry of the flow model. The individual parameters in the computer models used, should be checked and if necessary corrected (Fig. 19).

The target of future research is the improvement of the computer models and the integration of new models for energy and geometry related characteristics of the heat transfer surface [8,9] as well as instationary pulsating flow [10].

## Acknowledgement

The financial support for this research work has been granted by “Deutsche Forschungsgemeinschaft (DFG)”.

## References

- [1] S. Krause, Fouling of heat transfer surfaces by crystallization and sedimentation, *Internat. Chem. Engrg.* 33 (1993).
- [2] M. Bohnet, W. Augustin, H. Hirsch, Influence of fouling layer shear strength on removal behaviour, in: T.R. Bott, et al. (Eds.), *Understanding Heat Exchanger Fouling and its Mitigation*, United Engineering Foundation and Begell House, New York, 1997, pp. 201–208.
- [3] FLUENT 5, Users’s Guide, Vol. 2.
- [4] A.R. Konak, A new model for surface reaction-controlled growth of crystals form solution, *Chem. Engrg. Sci. Bd.* 29 (7) (1974) 1537–1543.
- [5] J. Lammers, *Zur Kristallisation von Calciumsulfat bei der Verkrustung von Heizflächen*, Diss. TU Berlin, 1972.
- [6] M. Bohnet, Fouling of heat transfer surfaces, *Chem. Engrg. Technol.* 10 (2) (1987) 113–125.
- [7] N. Epstein, Fouling of heat exchangers, *Chem. Pub. Corp.* (1983), ICHMT Symp., 1981, Dubrovnik.
- [8] M. Förster, W. Augustin, M. Bohnet, Influence of the adhesion force crystal/heat exchanger surface on fouling mitigation, *Chem. Engrg. Proc.* 38 (1999) 449–461.
- [9] M. Förster, M. Bohnet, Modification of molecular interactions at the interface crystal/heat transfer surface to minimize heat exchanger fouling, *Internat. J. Therm. Sci.* 39 (2000) 697–708.
- [10] M. Förster, W. Augustin, M. Bohnet, Anti-fouling strategies, in: *Proceedings of the 3rd European Thermal Sciences Conference*, 2000, Heidelberg, Germany.